# Compensating for Intraoperative Soft-Tissue Deformations Using Incomplete Surface Data and Finite Elements

David M. Cash, Michael I. Miga*, *Member, IEEE*, Tuhin K. Sinha, Robert L. Galloway, and William C. Chapman

***Abstract*—Image-guided liver surgery requires the ability to identify and compensate for soft tissue deformation in the organ. The predeformed state is represented as a complete three-dimensional surface of the organ, while the intraoperative data is a range scan point cloud acquired from the exposed liver surface. The first step is to rigidly align the coordinate systems of the intraoperative and preoperative data. Most traditional rigid registration methods minimize an error metric over the entire data set. In this paper, a new deformation-identifying rigid registration (DIRR) is reported that identifies and aligns minimally deformed regions of the data using a modified closest point distance cost function. Once a rigid alignment has been established, deformation is accounted for using a linearly elastic finite element model (FEM) and implemented using an incremental framework to resolve geometric nonlinearities. Boundary conditions for the incremental formulation are generated from intraoperatively acquired range scan surfaces of the exposed liver surface. A series of phantom experiments is presented to assess the fidelity of the DIRR and the combined DIRR/FEM approaches separately. The DIRR approach identified deforming regions in 90% of cases under conditions of realistic surgical exposure. With respect to the DIRR/FEM algorithm, subsurface target errors were correctly located to within 4 mm in phantom experiments.**

***Index Terms*—Deformation identification, finite element modeling, organ deformation, registration.**

## I. Introduction

THE goal of image-guided surgery (IGS) is to provide the surgeon with accurate spatial information regarding the location of pathology in real time during the procedure. In many image-guided systems, this navigational assistance is provided by a rigid alignment between the coordinate system associated with the preoperative tomographic images and patient anatomy. Frequently, the registration is established by matching corresponding rigid anatomical landmarks or extrinsic fiducials [1]–[3]. However, during open abdominal procedures to resect liver tumors, no such rigid point-based features exist.

Manuscript received July 12, 2004; revised June 29, 2005. This work was supported in part by the National Institutes of Health (NIH) under Grant R33-CA91352. The Associate Editor responsible for coordinating the review of this paper and recommending its publication was D. Hawkes. *Asterisk indicates corresponding author.*

D. M. Cash, T. K. Sinha, and R. L. Galloway are with the Department of Biomedical Engineering, Vanderbilt University, Nashville, TN 37235 USA.

*M. I. Miga is with the Department of Biomedical Engineering, Vanderbilt University, Nashville, TN 37235 USA (e-mail: michael.i.miga@vanderbilt.edu).

W. C. Chapman is with the Department of Surgery, Washington University School of Medicine, St. Louis, MO 63110 USA.

Digital Object Identifier 10.1109/TMI.2005.855434

The common assumption that the organ is rigid has been shown not to hold true in many cases, and soft tissue deformation is often present. In neurosurgery, the phenomenon is known as brain shift, and has been well documented [4]–[8]. Despite the rigid confines of the cranium, the degree of nonrigid brain deformation has been shown to compromise the fidelity of IGS navigation. There is little doubt that for IGS to evolve toward other applications, the need to account for soft tissue deformation is important.

While rigid registrations align the two coordinate systems globally, nonrigid methods are employed to account for displacements that occur on a local scale. Many studies use a calculation based on the closest point distance to determine correspondence and drive a nonrigid transformation. Szeliski and Lavallée [9] model displacements between two surfaces with a volumetric B-spline. The transformation is optimized according to a cost function based on the closest point distance and a regularizing term. Audette *et al.* [10] use recursive smoothing splines with the iterative closest point (ICP) method to track cortical surface deformations based on regularly spaced range scan data. Chui and Rangarajan developed an iterative solution for recovering nonrigid movement between two point sets using a thin plate spine transform [11].

Other methods augment correspondence functions with intrinsic surface properties, such as curvature, to extract nonrigid motion. Augmenting the corresponding function with curvature and principal frames, Feldmar and Ayache [12] propose a hierarchical approach: first with a globally rigid alignment, then globally affine, and finally locally affine transformations. Laskov and Kambhamettu [13] use an affine motion model by minimizing a linear set of equations based on the change of Gaussian curvature. Their study relies on the assumption that the surface can be represented with an orthogonal parametrization, and it extends upon a similar algorithm, which estimated nonrigid motion using surface normals [14]. Meier [15] also works with parameterized surfaces, building correspondence functions based on distance, surface normals, and curvature to determine an appropriate warping of parameter space between two objects. Shi *et al.* [16] calculated bending energies based on the principal curvatures of surface points. The bending energies were then used to define a deformation field and track motion of the left ventricular wall. Aylward [17] developed a unique correspondence metric that matches geometric features to image intensity values, and used this metric to align representations of the liver vasculature acquired from intraoperative ultrasound and preoperative tomograms.

Most of these studies calculate nonrigid alignments under the basic assumption that both data sets contain a complete description of the surface. However, only sparse and often incomplete intraoperative data is available due to time or access constraints. Research has been done to register sparse intraoperative data from ultrasound to preoperative images of the liver using statistical models [18] and voxel-based intensity methods [19]. These methods have been used in minimally invasive procedures to account for motion and deformation in the liver caused by respiration. With the unpredictable nature of deformation that arises in open abdominal procedures, some assumptions must be made regarding the regions of surface data that are unavailable in the intraoperative set.

An alternative strategy in compensating for deformation is to model the underlying biomechanics using the finite element method (FEM). In related image-guided surgical research, FEM has been used to account for intraoperative deformations. Miga and Paulsen constructed a model to accurately predict the effects of gravity [20], pharmacological agents [21], and surgical events [22] on the brain. Ferrant *et al.* [23] used FEM in a more interpolative sense, determining deformation between a preoperative tomogram volume and serial intraoperative magnetic resonance (MR) images. However, their work did not concentrate on the use of sparse intraoperative data, but rather focused on augmenting iMR methods. Skrinjar [24] acquired sparse surface data points from stereo pair images of the exposed cortical surface during surgery and used a discrete model to account for displacements due to brain shift. Lunn *et al.* [25] created "control points" from ultrasound data and used a weighted combination of FEM solutions based on correlating these points with model calculations.

In contrast to the neurosurgical setting, the dynamics of liver surgery hold different challenges with respect to the application of IGS techniques. For example, in the case of open abdominal liver surgery, often the surrounding ligaments are removed to better visualize and inspect the organ for the removal of tumors. In addition, the liver is routinely adjusted, i.e.,"packed," for stabilization resulting in significant organ deformation when compared to its preoperative CT images. Due to the robust physiological and homogeneous constitution of the liver, tumor resections routinely involve resection margins on the order of 1 cm. Studies have shown that lower recurrent rates are achieved when this 1-cm margin of tumor-free liver parenchyma is achieved in the resection [26]. Thus, for image-guidance to be effective in liver resections, it must produce a TRE of $\leq 1$ cm. Unlike the neurosurgical environment where the cranium confines the brain at the initial stages of surgery, a significant amount of tissue deformation during liver surgery occurs at the beginning. From the perspective of compensation, a strategy to account for the initial deformations associated with surgical presentation would be a significant contribution to the application of IGS techniques to intra-abdominal liver surgery. Using conventional rigid registration methods that minimize error metrics based on Euclidean distance (such as the rigid version of the ICP algorithm), deformation can be misinterpreted as rigid registration error. If this occurs, deformed areas may become better aligned at the expense of misregistering minimally deformed areas. An example of this phenomenon is shown in Fig. 1.

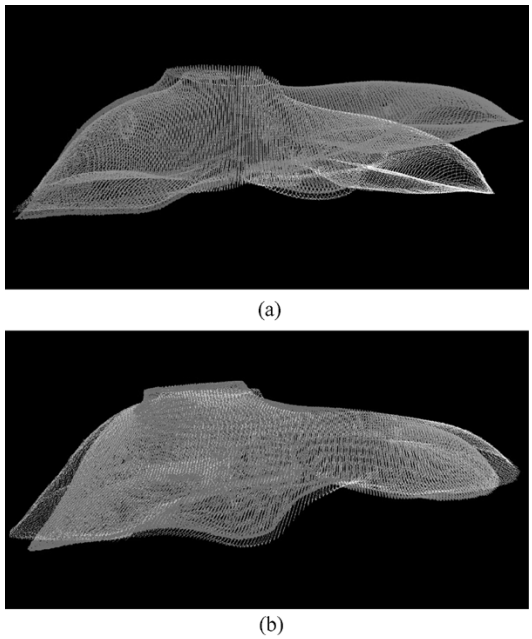

Fig. 1. (a) With a deformation present, (b) rigid registration procedures, such as ICP, will attempt to minimize the global error metric, which could cause some nondeformed areas to become misregistered.

Although the work within the neurosurgical environment has been encouraging, these techniques are not completely amenable to addressing the challenges associated within image-guided liver surgery. We have performed several initial investigations into the reality of applying image-guided techniques for the liver. Some initial work regarding the image alignment for liver surgery focused on assessing liver surface registrations [27] using the ICP algorithm by Besl and McKay [28]. Within this work, a liver phantom was segmented from the CT image volume and aligned with data acquired by swabbing the liver phantom surface with an optical digitizer. The results indicated a fiducial and TRE of approximately 3 mm in both cases; however, these studies did not investigate the effects of deformation. Related studies using an optically tracked laser range scanner to accomplish the same task reported registration errors less than 2 mm in phantoms. Phantom experiments were repeated in the presence of deformation and showed a distinct increase in target error (as high as 7.7 mm). To assess feasibility of the range scanner in the operating room, an in vivo case demonstrating the registration of an intraoperative liver range scan to the preoperative computed tomography (CT) image volume was presented and showed good qualitative agreement in alignment [29]. Some preliminary work has also been forthcoming regarding the nonrigid registration of the image volume using laser range scanning data [30]. In this work, the closest point operator was used to adjust a finite element model of the preoperative liver to match the intraoperative conditions. The results demonstrated an enhanced alignment to that achieved in the rigid registration associated with [30].

The study presented within this paper represents important advances over the initial work presented in [30], [31]. More specifically, a novel two step algorithm is proposed which improves the boundary correspondence by first providing a deformation-identifying rigid registration (DIRR) followed by a nonrigid align-

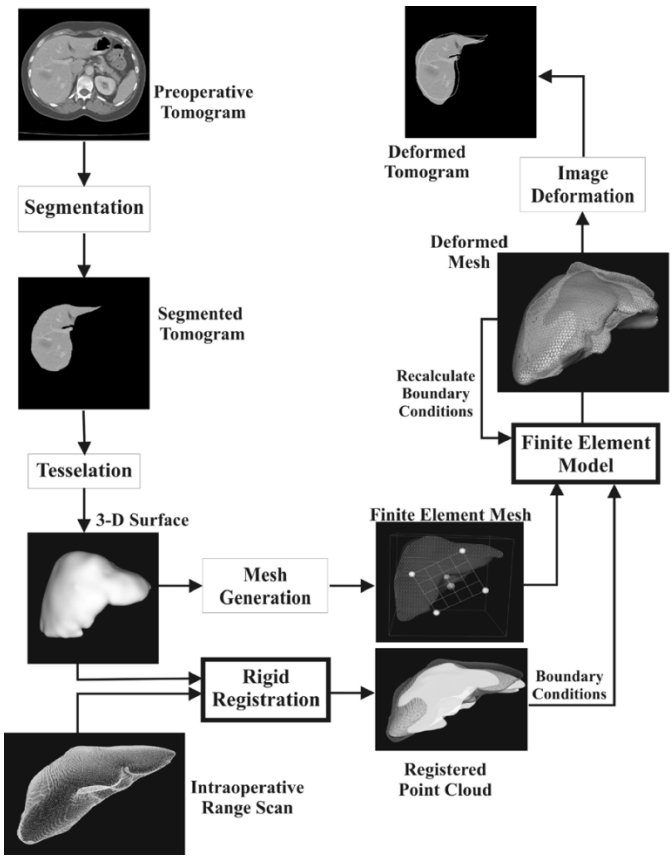


Fig. 2. Overview of the MUIGLS process.

ment using an incremental finite element approach. These advances have two important aspects: 1) the DIRR serves to distinguish areas of deformation to assist in generating proper correspondence in the applied boundary conditions; 2) the incremental finite element approach resolves geometric nonlinearities better than the previous work in [30]. The results describe a new set of phantom experiments to test the two step approach, which is called model updated image guided liver surgery (MUIGLS), and demonstrates an increased fidelity in alignment.

## II. Methods

### A. Overview

Fig. 2 shows a graphical overview of MUIGLS. The details of the individual steps in MUIGLS will be described in detail in the subsequent sections. Preoperative image data is acquired of the patient's abdomen using CT or MR scans. From these preoperative scans, the liver is segmented, and a three-dimensional surface is tessellated. This surface is used to determine a rigid alignment with respect to the intraoperative range scan data. Rather than perform this registration using the traditional ICP method, we developed a new form of alignment that weights regions of the data that are minimally deformed. The tesselated surface also serves as the input for generation of a tetrahedral volumetric mesh that will be the basis for a finite element model. Before running the FEM, boundary conditions are constructed based on the rigidly registered intraoperative data. The closest point distance between a boundary node of interest and the intraoperative, deformed surface is calculated. Execution of the model is repeated in an incremental fashion. Rather than using the entire closest point distance, a fraction of this value is used to prescribe the displacement boundary condition on the node. Each successive solution of the model updates the location of the mesh nodes, which triggers the calculation of new correspondences and boundary condition values. The model is repeated until the root mean square (RMS) closest point distances for all boundary nodes using the closest point boundary condition has reached some predetermined value. The results from the FEM are used to warp the preoperative image to match the intraoperative presentation.

Before explaining the methods used in MUIGLS, it is necessary to state some of the assumptions regarding image-guided liver surgery. From the authors' experience observing procedures in the operating room, the liver is assumed to be an elastic substance. Unlike neurosurgery, there are no apparent fluid effects in the organ, so there is no shrinking or swelling and volume is preserved. The most obvious feature of the deformation appears to be a shape change, where one region of the liver surface changes relative position with respect to another region. Often the deformation can be concentrated in a central region of the liver whereby a significant amount of semi-rigid translation and rotation is experienced by areas in the organ periphery, i.e., a lever-arm effect occurs due to significant deformations located more central to the organ. Translational effects due to forces such as diaphragm motion have been discussed in previous research [32]–[37] and are taken into account by employing breath-hold protocols [29]. During the surgery, the liver may change shape because of manipulation by the surgeon or resection, and this will warrant a new registration. At that point, the laser scanner will acquire a new intraoperative surface, so that the registration and deformation compensation can be recomputed. "Minimally deformed" areas are considered to be those which undergo deformation no greater than a few millimeters as determined by visual inspection. It is our goal in MUIGLS to reduce the amount of error from large scale deformations (1–4 cm) below the previously stated 1 cm level of target registration accuracy while not causing additional error seen in the minimally deformed regions.

### B. Data Representation

Phantom studies were performed on a poly (dimethyl) siloxane (rubber silicone) model of the liver, which is attached to a plexiglass base. Two sets of point-based landmarks are used for the study. Surrounding the outskirts of the phantom are vertical cylinders also attached to the vertical base, where seven white Teflon spheres have been placed in machined holders at the cylinder tops to serve as fiducials for a point-based registration. Inside the liver are mock tumors made of styrofoam, which are spherical with a radius on the order of 1–1.5 cm. The intensity of these tumors is approximately 20 times lower than the surrounding phantom, allowing for the tumors to be easily segmented with a simple region growing algorithm. The centroids of these tumors will serve as subsurface targets for accuracy studies. The position of the targets within the phantom are shown in Fig. 3. To induce a deformation in the phantom, an object of height 38.0 mm is placed underneath a region of the model. A large nylon screw pinned down other regions of thephantom and kept them stationary. Two different sites were

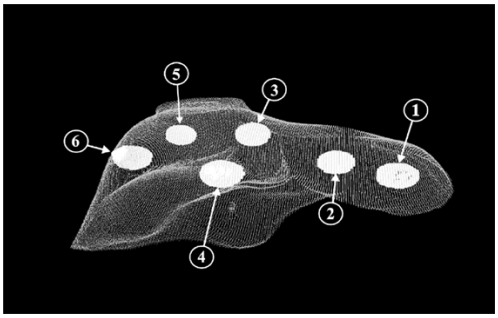


Fig. 3. Segmented CT surface of the liver phantom with subsurface tumors. The labels for each tumors are used as a reference for the results.

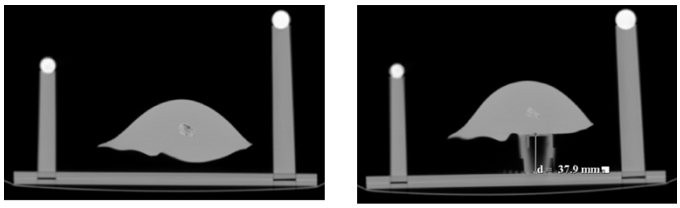


(a) (b)

Fig. 4. Corresponding CT slices from (a) nondeformed and (b) deformed image. The plastic object placed below the liver produces the deformation observed in Fig. 1(a). The height of the object is approximately 38 mm.

chosen for deformation. We chose these locations to mimic some of the physical manipulations that a surgeon may perform during a procedure. The first deformation occurred under the left lobe, where tumors 1 and 2 experienced the most shift, while the second site was at the middle of the inferior ridge, underneath segments III, IV, and V as defined by Couinaud [38]. For this case, the largest shift occurred at tumors 4 and 6. CT scans and range scans were taken while the phantom was in the nondeformed state and for each one of the deformed states. Corresponding slices from the nondeformed tomogram and one of the deformed volumes are shown in Fig. 4.

### C. Identification of Deformation

The first novel step in MUIGLS is the rigid alignment between the preoperative and intraoperative coordinate systems. While conventional rigid registrations are relatively easy to implement, they are also susceptible to misalignment caused by deformation. It would be possible to reduce the effects of deformation on rigid registration by identifying areas that are minimally deformed and using only landmarks in these regions for the registration.The effects of identifying minimally deformed regions can be illustrated with the ICP algorithm, a common method of registering two surfaces. ICP relies on the closest point distance metric. For the $i^{th}$ point in data set $X$, the closest point distance $d_{cp,i}$ is defined as the minimum distance from this point to a landmark in the other data set $Y$

$$d_{cp,i} = d(X_i, Y) = \arg\min_{y \in Y} \text{dist}(X_i, y). \tag{1}$$

In the ICP algorithm, the RMS residual of closest point distances over the entire surface is the cost function that is minimized through the iterative process. However, more information can be obtained when examining a histogram of the signed distance value distribution at a given alignment, as seen in Fig. 5.

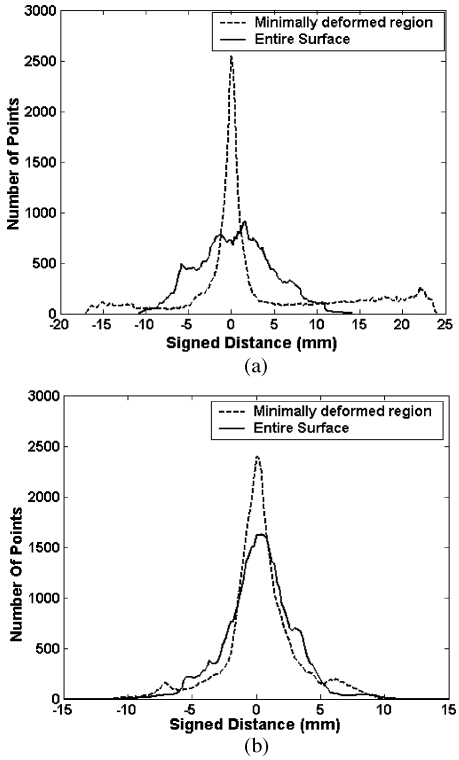


Fig. 5. Histogram of signed distance distribution for rigid alignments between a nondeformed surface and the surface deformed at (a) the left lobe and (b) the inferior ridge. The solid line indicates that the alignment is performed by registering the entire surface with the ICP algorithm. The dashed line is acquired with the same registration method, but this time only regions of the surface that were visually identified as "minimally deformed" are used in the registration.

The signed distance indicates how far a point is outside of the surface (positive) or inside (negative). In this figure, the alignments were obtained using ICP: one scenario used the entire surface in the registration, while the other used only areas that were visually identified as minimally deformed. When using the entire surface in the registration, the signed distance histogram has a narrow band of values distributed in a relatively uniform fashion, as displayed by the solid lines in Fig. 5. When only the minimally deformed regions are registered using ICP, the histogram of signed distances has a much sharper peak at the histogram bins closest to zero, as indicated by the dashed lines. This alignment also produces a larger range of distance values that are associated with the deformed areas observed in Fig. 1(a) and play no role in this selective ICP alignment.

Often, information about the surface regions which are minimally deformed is not available *a priori*. We developed a DIRR algorithm that aligns two surfaces according to the minimally deformed areas without any manual identification of these regions. For each point $i$ in the $N_S$ points of intraoperative data, a signed distance, $d_{s,i}$, to the nondeformed surface is calculated. These distance values are then used in the following cost function:

$$f(S) = \sum_{i=1}^{N_S} \exp\left(\frac{-{d_{s,i}}^2}{(2\tau^2)}\right). \tag{2}$$

The gaussian term is similar to one used for fuzzy correspondence in the work of Chui *et al.* [11]. As more points approach

a closest point distance of zero, the output value of the cost function will increase. At the same time, this cost function will not cause significant penalties for points which have large signed distances to the target surface that are associated with deformation. The parameter that controls the behavior of the cost function is the standard deviation of the gaussian function, $\tau$. This parameter usually ranges between 0.5 – 2.0 mm. Currently, the cost function is optimized using Powell's method [39] as implemented in the VXL library [40]. The parameters for the optimization are the six degrees of freedom that represent the rigid transformation that is applied to the intraoperative data. Unit quaternions represent the rotation.

In many cases, it is necessary to speed up calculations and provide smoother objective functions. The underlying surfaces of segmented preoperative data and intraoperative data were represented by radial basis functions (RBFs). A biharmonic RBF was used to interpolate the signed distance between any point in three dimensional space and the surface [41]. The zero isocontour from the resulting RBF function represents the fitted surface. To make this method computationally efficient for large data sets, a special implementation which provides for the fast evaluation and solution of RBFs was used, developed by FarField Technology (FastRBF, Far Field Technology, Christchurch NZ).

To test the DIRR algorithm, points sets from the deformed range scan and CT data were registered to the minimally deformed surfaces. These areas were manually designated from the surface by visual inspection and knowledge regarding the location of the object deforming the phantom. The minimally deformed areas were the only points used in an ICP registration, which served as a "ground truth" alignment to produce the same effect in the closest point histogram distribution as observed in Fig. 5. Then, the DIRR was performed without the aid of identifying the deformed surfaces. The results were compared to the ground truth using the six subsurface targets representing the tumor centroids. Like many registration algorithms, the DIRR needs an initial guess that roughly aligns the two surfaces. The initial alignment is achieved by identifying four landmarks on the phantom surface to serve as fiducials in a point-based registration.

To test the sensitivity of the DIRR to initial alignment, the position of each fiducial was randomly perturbed up to 1 cm away from its original position for 1000 trials. The results from the DIRR were compared against the ground truth and categorized as either a success or a failure. A success was defined as any registration where all tumor errors were less than 5.0 mm, which was confirmed by visually inspecting the resulting alignment.

### *D. Deformation Correction Using Finite Element Modeling*

After the rigid alignment between the two coordinate systems has been established, the next step is to model the deformation using a finite element model. The mesh used in the model is constructed from the preoperative tomographic volume, which represents the nondeformed state of the organ. The first step in mesh generation is to segment the liver from the rest of the abdomen. Segmentation is performed either manually or using a semi-automatic method *et al.* [42], [43] that is a modification of the level-set method. The manual segmentation requires many hours to perform, while the level-set method can usually be completed in 30 min to 1 h. From the segmented organ volume, a surface is tesselated using either the marching cubes method [44] or the aforementioned surface fitting algorithm using RBFs. The surface is represented as a set of polygons and serves as input to the mesh generation software [45]. This software uses the boundary description to generate a tetrahedral grid volume of the entire liver shape.

The deformation of the liver is modeled using a linear stress-strain relationship for an isotropic, three-dimensional solid. If we assume static equilibrium, then

$$\nabla \cdot \sigma = \mathbf{B} \tag{3}$$

where $\sigma$ is the stress tensor and $\mathbf{B}$ is the body force vector. Stress can be related to strain by the following relationship:

$$\sigma = C\varepsilon \tag{4}$$

where $C$ represents the material stiffness matrix. For a Hookean solid, $C$ depends on two properties, Young's Modulus, $E$, and Poisson's ratio, $\nu$. The displacement vector, $\mathbf{u}$, is the value that will be solved for, and it is related to normal strain $\varepsilon$ and the shear strain $\gamma$ by

$$\varepsilon_x = \frac{\delta u_x}{\delta x}, \varepsilon_y = \frac{\delta u_y}{\delta y}, \varepsilon_z = \frac{\delta u_z}{\delta z} \tag{5}$$

$$\gamma_{xy} = \frac{\delta u_x}{\delta y} + \frac{\delta u_y}{\delta x}, \gamma_{xz} = \frac{\delta u_x}{\delta z} + \frac{\delta u_z}{\delta x}, \gamma_{yz} = \frac{\delta u_y}{\delta z} + \frac{\delta u_z}{\delta y} \tag{6}$$

where $\mathbf{u} = \{u_x, u_y, u_z\}$ is the cartesian displacement. By combining (3)–(6), a system of partial differential equations can be expressed in terms of the displacement vector, $\mathbf{u}$, to form the Navier equation

$$\frac{E}{2(1+\nu)}\nabla^2 \mathbf{u} + \frac{E}{2(1+\nu)(1-2\nu)}\nabla(\nabla \cdot \mathbf{u}) = \mathbf{B}. \tag{7}$$

The partial differential equation is solved using the Galerkin weighted residual technique with linear basis functions. The system of equations that solves for the displacement vectors at every node in the mesh can be written as

$$[K]\{\mathbf{u}\} = \{\mathbf{b}\}. \tag{8}$$

One fundamental component to employing the finite element method is the prescription of boundary conditions. These boundary conditions are derived from knowledge of the forces applied to the liver within surgery as well as information from the intraoperative data. There are three different types of boundary conditions implemented in the model. The first set of boundary conditions are categorized as "fixed," a set of Dirichlet conditions representing immobile regions of the organ. Typically, obscured regions of the right lobe that rest against other parts of the viscera belong to the fixed category. "stress-free" boundary conditions are the second category, which represent regions unrestricted by force. The final type will be referred to as "closest point" boundary conditions. These nodes play the most significant role in modeling the deformation and are considered a mixed boundary condition,

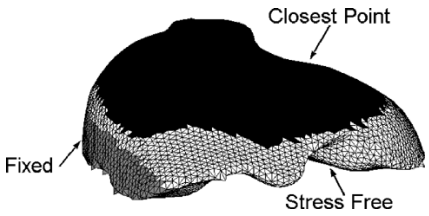


Fig. 6. Example set of boundary conditions for the liver phantom mesh. The dark grey represents the boundary nodes that obey the mixed "closest point" boundary condition formulation. The medium grey value denotes fixed regions, while the light grey boundary conditions are stress free.

in that, of the 3 vector components, one component is Dirichlet while the remaining two are Neumann conditions. An example of how the different regions of the organ are classified according to boundary condition type is illustrated in Fig. 6.

The details in implementing the "closest point" boundary conditions are critical to successfully recovering the deformation in our approach. It should be noted that the initial DIRR is also integral to the prescription of boundary conditions; i.e., at the initiation of deformation, the closest point distances will be directly related to the DIRR registration. Furthermore, with such a large amount of deformation present intraoperatively, improper correspondence can lead to boundary conditions that would cause improper nonrigid alignments and unrealistic distortions of the organ shape.

In our approach, two measures are taken to avoid improper correspondence when setting the displacements for the boundary conditions: 1) manipulation of the finite element equations such that the equations are sensitive to the organ surface geometry; 2) implementation of incremental solutions with a moving grid. The first involves modifying the conventional finite element method such that the weighted residual vector equations at the boundary are expressed in a coordinate reference that is designated to have one coordinate axis normal to the organ surface and the remaining two being tangent to that surface (as opposed to traditional Cartesian coordinate references). With respect to modeling anatomical organs and their deformations, there are some aspects to the application of boundary conditions that are particularly challenging to traditional Cartesian representations. For example, in the application of displacement boundary conditions to the liver, it is often desirable to express the movement of the boundary in a direction that is relative to the geometric shape, i.e., the coordinate system associated with directions that are approximately normal and tangential to the organ surface. One strategy is to take the desired normal displacement and convert this to its Cartesian counterparts, i.e.,

$$\begin{Bmatrix} dn \\ dt_1 \\ dt_2 \end{Bmatrix} = \begin{bmatrix} \vec{x}\cdot\vec{n} & \vec{y}\cdot\vec{n} & \vec{z}\cdot\vec{n} \\ \vec{x}\cdot\vec{t_1} & \vec{y}\cdot\vec{t_1} & \vec{z}\cdot\vec{t_1} \\ \vec{x}\cdot\vec{t_2} & \vec{y}\cdot\vec{t_2} & \vec{z}\cdot\vec{t_2} \end{bmatrix} \begin{Bmatrix} dx \\ dy \\ dz \end{Bmatrix} \tag{9}$$

where $\vec{n}$, $\vec{t_1}$, and $\vec{t_2}$ represent an orthogonal coordinate system with the normal (to the organ surface) and tangential axes, respectively. In this case, the inverse relationship in (9) would be used since the transformation shown is from Cartesian to normal-tangential space ($n$-$t$ *space*). In these equations, the application of a displacement normal to an organ surface can be achieved; however, the ability to relate mixed boundary conditions within the $n$-$t$ *space* framework is not possible using (9). For example, it may be desirable to allow an organ surface to slide along a supporting wall yet not deform in a direction normal to the wall, i.e., through the wall. In another situation, the deformation may need to be applied in a direction normal to the organ surface yet allow for sliding of tissue along the displacing surface (e.g., depressing the organ with a smooth object like a retractor). This type of boundary condition requires stress-free conditions tangent to the direction of constraint/motion and restricted normal displacements, e.g.,

$$\sigma_{t1} = \sigma_{t2} = 0,\ u_n = 0\ (\text{or}\ \alpha * d_{cp,i}) \tag{10}$$

where $\sigma_{t1,t2}$ are stresses applied tangent to the organ surface, and $u_n$ is a displacement normal to the surface. In this instance, the framework described in (9) cannot achieve these degrees of freedom in organ movement behavior.

A better approach than (9) is to rotate the equations of equilibrium for nodes concerned with the boundary into an $n$-$t$ *space* coordinate reference. This process usually involves the use of rotational matrices (sensitive to the organ boundary) being applied at the local element assembly level

$$[R]_i[K]_i[R^T]_j\{u\}_j = [R]_i\{b\}_i \tag{11}$$

where the premultiplication by $[R]_i$ on the left and right-hand side rotates the equilibrium equation and body force components ($[R]_i$ is the matrix shown in (9) and would be associated with the normal and tangential coordinates reference of the $i^{th}$ node), and the $[R^T]_j$ multiplication rotates the displacement coefficients from Cartesian to $n$-$t$ *space* (i, j refer to $i^{th}$ weighted residual equation, and $j^{th}$ displacement coefficient, respectively). Careful attention must be paid to the determination of the rotational matrix, $[R]$, and to the arrangement of rotational multiplications (note, that $[R^{-1}]$ is orthogonal and equivalent to $[R^T]$). This approach to $n$-$t$ *space* calculation has been reported by Engelman *et al.* [46]. Based on our experience with realistic anatomical deformations in the brain and liver, this type of boundary condition formulation has great utility in prescribing tissue-mimicking deformations [20], [30]. With respect to our approach, the "closest point" boundary condition is of the form expressed in (10) and is only possible through the formulation described by (11). More specifically, in these surface regions, the liver is prescribed to deform normal to the organ surface a designated amount (based on a fraction, $\alpha$, of the closest point distance, $d_{cp,i}$) and is also allowed to slide tangentially to accommodate that motion.

The second measure to improve correspondence involves an incremental approach for the model-updating process. Our technique uses an incremental application of the displacement boundary conditions in conjunction with a moving grid. The displacement increment size is not fixed; but rather, it is based on an attenuation of the value obtained from the closest point operator, which is recalculated before each incremental solution of the model. The advantages of this approach are that it avoids geometric nonlinearities and provides more realistic deformations by recalculating the surface normals based on the current deformed grid. Others have used similar approaches in the brain and have found the incremental approach to moderately

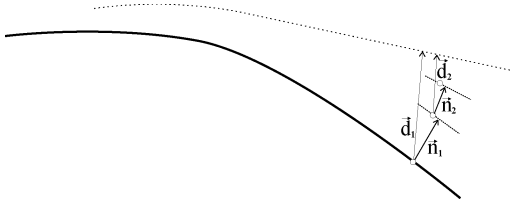


Fig. 7. Implementation of "closest point" boundary conditions using normal-tangential space. The closes point distance for the boundary node at increment 1, $\|\vec{d}_1\| = d_{cp,1}$, is determined. From $d_{cp,1}$, a normal distance, $\|\vec{n}_1\| = \alpha d_{cp,1}$, is computed for use in the "closest point" boundary condition where $\alpha$ is the solution scale fraction that scales the closest point distance in the incremental framework. The new position of the boundary node, denoted by the small circle, lies on a plane that is a distance of $\alpha d_{cp,1}$ along the direction $\vec{e}_{n_1}$ away from its original location. The mixed formulation of the "closest point" boundary condition shown in (10) gives the node freedom to slide along this plane through the stress-free boundary conditions imposed on the two tangential axes. The same process is repeated for the second and subsequent increments.

improve the fidelity of their deformation modeling [47]. Our method is unique in that the moving grid is being used within the updates to calculate new surface normals and closest point distances. Currently, a stopping criterion used to halt the incremental updates is defined as the RMS distance to intraoperative data from all closest point boundary nodes. Once the average closest point distance is within 1–2 mm, a final increment is calculated and applied. Fig. 7 shows the relationship for the first and second increments of our approach. The closest point distance between the boundary node position at the time of the first increment and the intraoperative data is calculated $\|\vec{d}_1\| = d_{cp,1}$. The normal distance, $\vec{n}_1 = \alpha * d_{cp,1} * \vec{e}_{n_1}$, is calculated where $\alpha$ is the fraction by which the closest point distance is scaled, and $\vec{e}_{n_1}$ is the unit vector associated with $\vec{n}_1$. The "closest point" boundary conditions are then set with the attenuated closest point distance designated as a Dirichlet condition along the normal direction and stress-free conditions for the two tangential axes [see (10)]. After the finite element model is calculated, the new position of the node (small circle) will lie on a plane formed by the tangential axes. This plane will be a distance $\|\vec{n}_1\|$ away from the node's original plane. However, the node is not confined to reside along the normal due to the tangential stress-free conditions; therefore, the point to point distance is not required to equal $\|\vec{n}_1\|$. After the position has been updated, a new closest point distance $\|\vec{d}_2\| = d_{cp,2}$ and normal distance for the boundary condition $\vec{n}_2 = \alpha * d_{cp,2} * \vec{e}_{n_2}$ are calculated.

With respect to the solution at (8), a sparse format and iterative solver were implemented using the Portable, Extensible Toolkit for Scientific Computation (PETSc) package [48], which is capable of solving large linear systems in parallel. For these experiments, the matrix was preconditioned using an incomplete LU factorization and an iterative solver based on the generalized minimal residual (GMRES) method [49].

Experiments were performed on the phantom data in order to examine the effects of various parameters involved in the incremental approach. For every finite element experiment, the partial surface from a deformed range scan data set was used to drive the model. Target registration error (TRE), as defined in Fitzpatrick *et al.* [50], was calculated using the subsurface tumors. The target positions from the nondeformed mesh were updated through the model and compared to the actual positions obtained from the CT volume of the deformed organ.

TABLE I
INITIAL ALIGNMENT METHODS FOR INTRAOPERATIVE RANGE SCAN DATA IN THE FEM

| Alignment | Method | Non-deformed surface | Deformed Surface |
|---|---|---|---|
| FID | Fiducials | N/A | N/A |
| ICP-WHOLE | ICP | Complete CT | Complete CT |
| ICP-PARTIAL | ICP | Complete CT | Partial Range Scan |
| DIRR-WHOLE | DIRR | Complete CT | Complete CT |
| DIRR-PARTIAL | DIRR | Complete CT | Partial Range Scan |

The implementation of "closest point" boundary conditions is an important factor with regards to accurately localizing targets. The cartesian representation for this category of boundary conditions was tested against rotating the node into a local normal-tangential coordinate system and prescribing the mixed boundary conditions as described above. Another factor affecting the closest point calculations was the initial alignment that was used to transform the intraoperative data. As a result, five separate registration methods were used to provide the initial alignment prior to performing FEM model-based compensation. The methods are shown in Table I.

Since idle time is undesirable during surgery, the incremental finite element approach must be designed to be as expedient as possible. Computation time can be reduced through two measures. First, the number of increments can be decreased, which is achieved by increasing the solution scale constant responsible for attenuating the closest point distances before setting the boundary condition values, i.e., as the solution scale approaches unity, the number of increments will decrease. The second method for reducing computation time is to make every incremental execution of the model faster. Within each successive solution of (8), the majority of computation is devoted to rebuilding the stiffness matrix and recalculating the preconditioner, which are necessary due to the dynamic grid. These steps can be completely avoided after the first increment by using the original mesh for every iteration, updating the boundary nodes and conditions separately, similar to the approach of Platenik *et al.* [47]. In this manner, only the right-hand side is affected, and the individual solutions from each increment can be summed to determine the final displacements. When solving the model multiple times, the quality of the dynamic grid could degrade. To avoid a problem with mesh quality, the original mesh is used for each iteration, but the normals and boundary nodes are separately maintained and updated after each iteration. Since the normals vary, the rotation matrices will change and the stiffness matrix must be rebuilt. Thus, more computation time is likely required per incremental solution, but the original mesh structure is preserved, possibly enhancing performance of the solver by improving the condition number of the stiffness matrix in (8).

## III. RESULTS

### A. Deformation Identification

The "ground truth" for the rigid alignment involves manually identifying minimally deformed regions on the CT surface through visual inspection, and then using these regions in an ICP registration. When registering the minimally deformed region of

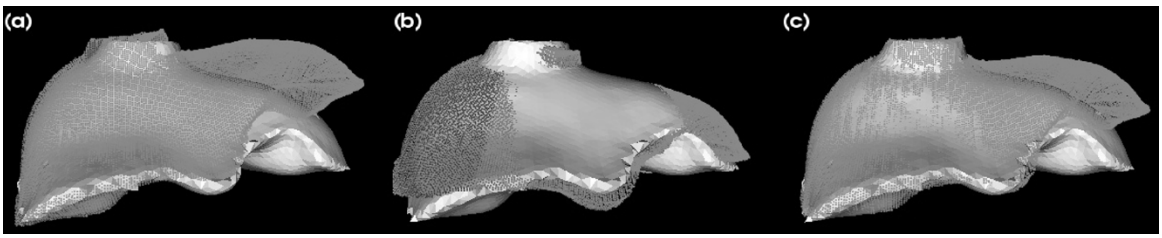


Fig. 8. Various alignments of intraoperative range scan of phantom with the preoperative surface: (a) Using the surrounding extrinsic fiducials, (b) Using the complete surface data with ICP registration, and (c) using only the manually identified minimally deformed regions for the ICP. It is (c) that will serve as the ground truth for experiments testing the DIRR algorithm.

the surface to the original volume, the RMS of the closest point distances was 0.9 mm ($\max \text{closest point distance} = 3.3\,\text{mm}$) for the first deformation case using approximately 10 000 points, and 1.0 mm ($\max = 3.4$) for the second deformation, where the partial surface contained approximately 8800 points. As a comparison, the RMS of the closest point distances was 4.2 mm ($\max = 14.3$) and 2.6 mm ($\max = 10.8\,\text{mm}$) for the two data sets when using the whole surface in the ICP registration. The differences between the fiducial registration, the whole surface ICP, and the "ground truth" alignment based on ICP using only the minimally deformed regions are displayed in Fig. 8. Fig. 8(c), displaying the ground truth, indicates a better alignment of the left side of the surface compared to the alignment obtained from the external fiducials.

To initialize the DIRRs optimization, four points representing landmarks on the surface were used for a fiducial-based registration. The fiducial registration error (FRE) is defined by the following equation [50]

$$\text{FRE} = \sqrt{\frac{1}{N}\sum_{i=1}^{N} |\mathbf{R}x_i + \mathbf{t} - y_i|^2} \tag{12}$$

where $N$ is the number of landmarks in point sets $x$ and $y$, and $\mathbf{R}$ and $\mathbf{t}$ are the rotation and translation parameters that represent the rigid registration. The FRE for these initial registrations were 5.8 and 5.3 mm for the two cases using deformed CT data and 5.8 and 8.5 mm for range scan data. Since it is difficult to localize surface landmarks with a high degree of precision or accuracy, the position of the landmarks was perturbed by a distance of up to 1 cm. From these random perturbations, the initial alignment given to the DIRR was varied over 1000 trials. Table II shows the results of the DIRR registration experiments, with trials classified as a "success" or "failure" based on the definition given in Section II-C. In all trials, the complete nondeformed surface from the CT data was used. For the deformed surface, columns two and three indicate the results when using complete surface data from CT volumes, and columns four and five display the results when using only the partial surface acquired from the range scanner.

TABLE II
RESULTS FROM THE DIRR ALGORITHM. THESE VALUES ARE THE MEAN DISTANCE, MM, FROM THE CENTROID LOCATION USING THE DIRR ALIGNMENT TO THE CORRESPONDING CENTROIDS AT GROUND TRUTH

| Deformation 1 | Complete CT | | Incomplete Range Scan | |
|---|---|---|---|---|
| | DIRR Success | DIRR Failure | DIRR Success | DIRR Failure |
| Trials | 999 | 1 | 903 | 97 |
| Tumor 1 | 1.6 | 26.4 | 3.6 | 19.2 |
| Tumor 2 | 1.2 | 19.2 | 2.9 | 15.0 |
| Tumor 3 | 0.5 | 11.2 | 1.8 | 7.6 |
| Tumor 4 | 0.7 | 7.2 | 0.9 | 5.0 |
| Tumor 5 | 0.5 | 9.7 | 2.5 | 4.1 |
| Tumor 6 | 0.8 | 9.4 | 1.4 | 4.3 |
| Mean | 0.9 | 13.9 | 2.2 | 9.2 |
| Deformation 2 | Complete CT | | Incomplete Range Scan | |
| | DIRR Success | DIRR Failure | DIRR Success | DIRR Failure |
| Trials | 1000 | 0 | 972 | 28 |
| Tumor 1 | 1.4 | N/A | 4.1 | 22.9 |
| Tumor 2 | 1.2 | N/A | 3.5 | 16.4 |
| Tumor 3 | 1.3 | N/A | 2.4 | 10.8 |
| Tumor 4 | 1.8 | N/A | 3.9 | 7.7 |
| Tumor 5 | 1.4 | N/A | 2.2 | 11.1 |
| Tumor 6 | 1.9 | N/A | 3.2 | 7.0 |
| Mean | 1.5 | N/A | 3.2 | 12.7 |

### B. Finite Element Modeling Experiments

The two material properties that describe a linearly elastic surface are Young's modulus, $E$, and Poisson's ratio, $\nu$. Both properties were varied to determine their effect on the model. Young's modulus did not affect the model while varying it between 30 and 400 kPa. This material property would have an impact if there was heterogeneity in the model, such as incorporating different material properties for stiff tumors. When varying Poisson's ratio between 0.3 and 0.495, the model did exhibit some change. The RMS distance between boundary nodes was 0.7 mm over the range of parameter values, with some individual nodes moving as much as 8.0 mm between solutions. The largest movement in the subsurface targets was 0.5 mm. While varying the properties did not significantly affect these modeling studies, they could play a larger role as the model becomes more advanced.

The solution scale, $\alpha$ of (10), is a constant that represents the fraction of the closest point distance used for the boundary condition values. Before every increment, the updated closest point distance is calculated for each node and then scaled by this constant. We tested the incremental FEM model with six different values for the solution scale constant, ranging from 0.05 to 1.0. Fig. 9 shows the effects of the solution scale on the model for the first deformation case when aligning the intraoperative range scan data with each of the initial rigid alignments listed in Table I on the intraoperative data. In the second deformation set, varying the solution scale produced no significant effect on the model. The relationship between solution scale and the number of increments is shown in Table III. To better understand the effects of the approaches highlighted in Table III with respect

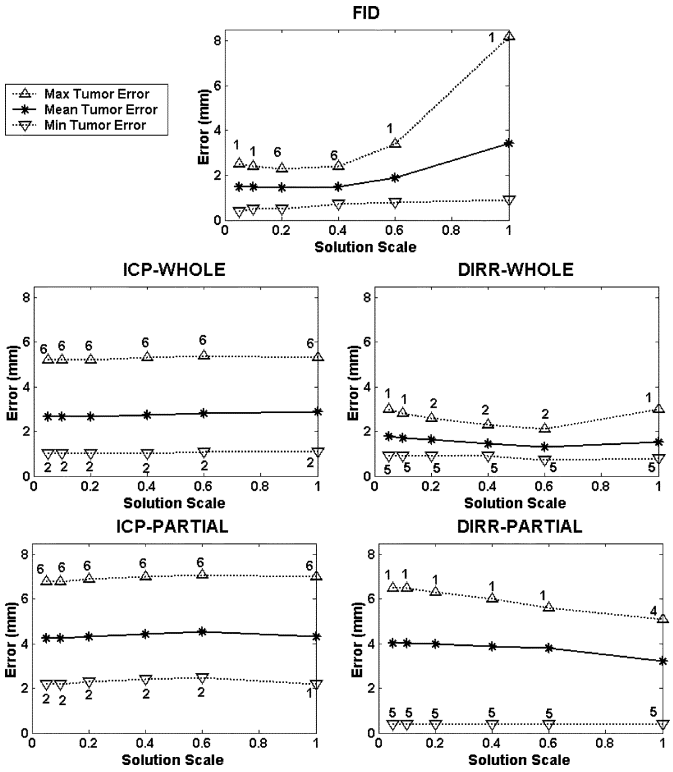


Fig. 9. Tumor error after modeling the first deformation case with varying solution scale. The mean error is plotted along with the minimum and maximum errors labeled with the tumor number from Fig. 3 where they occurred.

TABLE III
RELATIONSHIP OF THE SOLUTION SCALE WITH THE NUMBER OF FEM INCREMENTS

| Data Set | Registration | 0.05 | 0.1 | 0.2 | 0.4 | 0.6 | 1.0 |
|---|---|---|---|---|---|---|---|
| Deformation 1 | FID | 52 | 27 | 14 | 8 | 5 | 1 |
| | ICP-WHOLE | 27 | 14 | 8 | 5 | 4 | 1 |
| | ICP-PARTIAL | 29 | 15 | 9 | 5 | 4 | 1 |
| | DIRR-WHOLE | 45 | 23 | 12 | 7 | 5 | 1 |
| | DIRR-PARTIAL | 44 | 23 | 12 | 7 | 5 | 1 |
| Deformation 2 | FID | 41 | 21 | 11 | 6 | 5 | 1 |
| | ICP-WHOLE | 13 | 7 | 5 | 4 | 3 | 1 |
| | ICP-PARTIAL | 12 | 7 | 5 | 3 | 3 | 1 |
| | DIRR-WHOLE | 16 | 9 | 6 | 4 | 3 | 1 |
| | DIRR-PARTIAL | 18 | 10 | 6 | 4 | 3 | 1 |

to individual targets, Fig. 10 reports target error associated with each mock tumor shown in Fig. 3 (a solution scale of 0.2 was used for all results shown). The next set of experiments focused on the implementations of the boundary conditions and the stiffness matrix. While holding the solution scale fixed at 0.2 and using an initial alignment based on fiducials or ICP, the model was run, testing the normal-tangential description of boundary conditions against the cartesian boundary conditions. For both of these implementations, the model was tested using both a moving grid and a static grid. For the normal-tangential method, an additional test was performed to use the original static mesh, but to use updated closest points and normals. Ultimately, this requires rebuilding of the stiffness matrix with each increment. The results are shown in Fig. 11 (where the FID alignment was used) and Fig. 12 (ICP-PARTIAL alignment).

It is important to understand how the various components of the MUIGLS approach affect the localization of tumors.

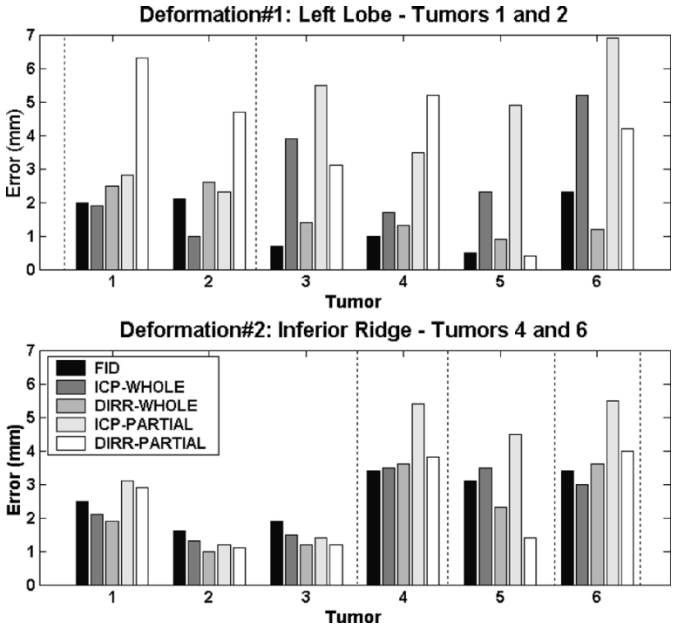


Fig. 10. FEM tumor errors with respect to the initial alignment. The solution scale used for these experiments is 0.2. The five alignment methods are listed in Table I. The dotted lines indicate the tumors experiencing the most deformation.

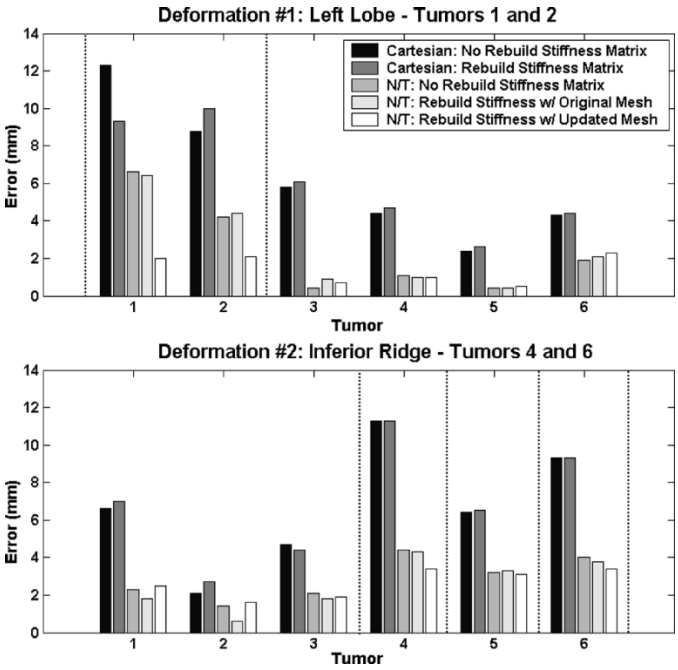


Fig. 11. Tumor errors from FEM model while varying implementation of boundary conditions and the construction method of the preconditioner and stiffness matrix. The initial rigid alignment used here was based on the external fiducials.

Table IV summarizes the effects of both registration and finite element modeling on target accuracy. The finite element modeling results come from the best scenario, where normal-tangential boundary conditions are used on a moving grid. In the column for the ICP-WHOLE alignment, the first deformation case yields a difference in the mean error when comparing the before and after model application. When employing the DIRR-WHOLE method, a more marked reduction occurs in the regions where the greatest amount of shift has

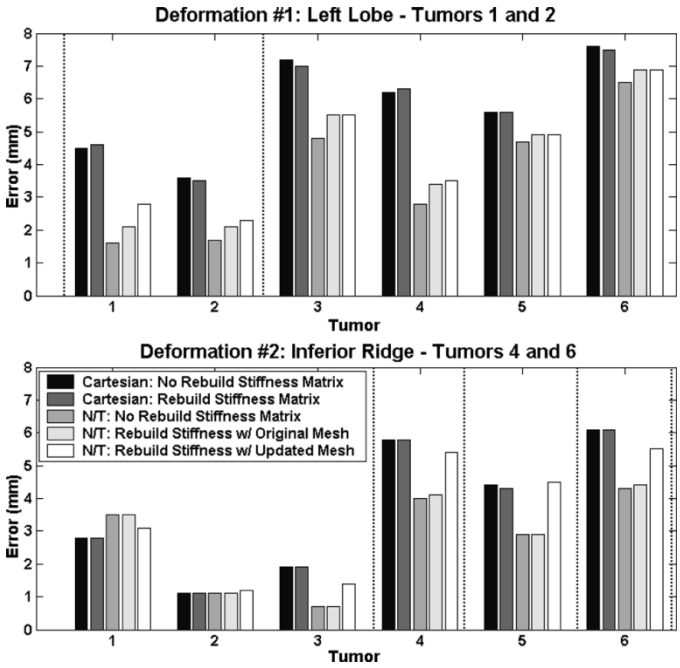


Fig. 12. Tumor errors from FEM model while varying implementation of boundary conditions and the construction method of the preconditioner and stiffness matrix. The initial rigid alignment used here was based on ICP of the range scan surface.

TABLE IV
IMPROVEMENT OF TUMOR ERROR, MM, AS A RESULT OF FINITE ELEMENT MODELING

(a) Deformation 1

| Tumor | ICP WHOLE | | DIRR WHOLE | | ICP PARTIAL | | DIRR PARTIAL | |
|---|---|---|---|---|---|---|---|---|
| | Before Model | After Model | Before Model | After Model | Before Model | After Model | Before Model | After Model |
| 1 | 6.6 | 1.9 | 32.6 | 2.5 | 7.0 | 2.8 | 33.3 | 5.6 |
| 2 | 4.9 | 1.0 | 21.3 | 2.6 | 6.8 | 2.3 | 22.0 | 4.2 |
| 3 | 8.0 | 3.9 | 2.0 | 1.4 | 8.4 | 5.5 | 4.2 | 3.1 |
| 4 | 6.3 | 1.7 | 1.6 | 1.3 | 8.1 | 3.5 | 6.5 | 5.3 |
| 5 | 2.5 | 2.3 | 1.2 | 0.9 | 5.4 | 4.9 | 0.6 | 0.4 |
| 6 | 6.0 | 5.2 | 0.6 | 1.2 | 8.0 | 6.9 | 3.9 | 4.2 |
| **Mean** | **5.7** | **2.7** | **9.9** | **1.7** | **7.3** | **4.3** | **11.8** | **3.8** |

(b) Deformation 2

| Tumor | ICP WHOLE | | DIRR WHOLE | | ICP PARTIAL | | DIRR PARTIAL | |
|---|---|---|---|---|---|---|---|---|
| | Before Model | After Model | Before Model | After Model | Before Model | After Model | Before Model | After Model |
| 1 | 2.9 | 2.1 | 1.9 | 1.9 | 3.5 | 3.1 | 3.3 | 2.9 |
| 2 | 1.8 | 1.3 | 1.6 | 1.0 | 2.0 | 1.2 | 1.6 | 1.1 |
| 3 | 1.3 | 1.5 | 1.7 | 1.2 | 1.9 | 1.4 | 1.2 | 1.2 |
| 4 | 4.3 | 3.5 | 4.6 | 3.6 | 5.3 | 5.3 | 4.2 | 3.8 |
| 5 | 3.8 | 3.5 | 2.8 | 2.3 | 4.1 | 4.5 | 3.3 | 1.4 |
| 6 | 4.2 | 3.0 | 5.8 | 3.6 | 6.1 | 5.5 | 6.8 | 4.0 |
| **Mean** | **3.0** | **2.5** | **3.0** | **2.3** | **3.8** | **3.5** | **3.4** | **2.4** |

occurred (tumors 1 and 2), as it has been identified by the DIRR. There are still improvements in the second deformation case, where the deformation is less significant.

## IV. DISCUSSION

### A. Deformation Identifying Rigid Registration

The most common form of determining correspondence is based on the closest point distance operator. For most surfaces and correspondence strategies, closest point distances are used as initial estimates of correspondence, allowing the iterative alignment of images to naturally bring points to their true one-to-one correspondence. With the presence of deformation, the closest point operator becomes less reliable as a means of determining correspondence. Many groups have proposed modifications to the closest point operator in order to achieve a more accurate correspondence estimate [11], [15], [16], [51]–[53].

Establishing correspondence with a closest point distance can be inaccurate when a large deformation is present. Rather than establish correspondence, the DIRR algorithm computes the signed distance to the underlying target surface, often represented by RBFs. The signed distance values are used to drive the gaussian term in the cost function (2), which rewards transformations where there are many points with small signed distances. When the cost function is at a maximum, it is associated with minimally deformed regions that are well-aligned. At the same time, the cost function does not penalize large signed distances associated with deformation.

The DIRR algorithm performs better when given a complete representation of the deformed surface. When perturbing each of the fiducials in the deformed set by 1 cm, there was only one failure in 1000 trials for the first deformation case while there were no failures for the second case. Both sets of trials came within 2 mm from the ground truth alignment. The partial surfaces from range scan surface data reach a successful alignment 90% of the time or greater. One strategy to improve success could be to use *a priori* information regarding the extent of deformation. Similar to our manually delineated deformation results, this information could be incorporated into DIRR semiautomatically, by manually classifying regions of the surface according to the confidence that deformation is or is not taking place. This confidence measure could be used to weight each point in the cost function accordingly.

Other sources of error regarding the DIRR include inaccuracies due to surface acquisition. These errors more than likely arise from range data acquisition and to a lesser extent the surface extracted from the segmentation of the tomograms. A discussion on the sources of error in range scans and how they pertain to image-guided surgery can be found in [29]. While the surface fit using the RBF data gets rid of some of the input noise, detail is lost as well. There is also the possibility that small regions of deformation (1–3 mm) are not being accounted for in either the partial ICP or DIRR algorithms, which is not in the scope of this study.

### B. Modeling Considerations

In most cases, the FEM model provides significant improvement over results from rigid registrations alone, as indicated by Table IV. The largest improvement in accuracy comes from rotating the boundary nodes into a normal-tangential coordinate system. By implementing mixed boundary conditions, which allow the nodes to move along the plane tangent to the surface, the results suggest that organ shift is better accommodated. When using the cartesian boundary conditions, the lack of interaction is observed by a distinct delineation where a transition of boundary condition types occurs, which is illustrated in Fig. 13. Specifying the displacement in the direction of the normal is intuitive if one were to examine the deformation from these experiments as a series of small increments. At every increment,

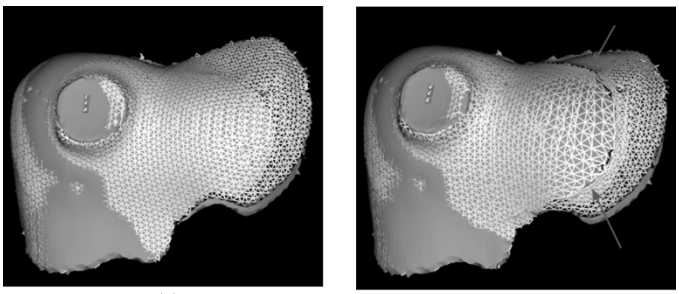

(a) (b)

Fig. 13. Quantitative comparison of closest point boundary conditions using the (a) normal-tangential local coordinate frame and (b) the cartesian coordinate frame. The cartesian boundary conditions result in a clear boundary between the closest point nodes and nodes that prescribe a different type of boundary condition. This boundary is highlighted by the red arrows in (b).

the actual displacement should closely align with surface normals. Allowing the node to freely move in the tangential direction resolves any discrepancies between the true direction of deformation and the one specified by the surface normal. However, unlike these phantom experiments, there might be a situation in which the deformation is not in the direction of the normals for the acquired intraoperative surface. At this point, the DIRR becomes more important. By identifying the deformation through the rigid registration, it would be possible to determine the vector that describes the orientation of the deformation with respect to the finite element mesh which could then serve in place of the mesh's surface normal.

Due to the incomplete nature of the intraoperative data acquisition, the initial rigid alignment used to set up the closest point boundary conditions also plays a significant role. In both deformation cases, the transformation obtained from the DIRR-WHOLE alignment provided very good results. However, when using an incomplete surface in the DIRR-PARTIAL alignment, small misalignments arise, especially rotations that were not recovered by the model and led to larger inaccuracies. The rigid fiducials from the images also provided good results, although the errors were lower in the first case, since there was little difference between the resulting registration and the one determined using DIRR. In both cases, the ICP algorithm did not perform as accurately as other alignments, since the alignment misregisters minimally deformed surfaces and eliminates the meaning of holding these areas fixed in the boundary conditions.

Given the time sensitive nature in the operating room and the significant costs that can be associated with running the finite element model numerous times, the selection of parameters for this model must focus on limiting the number of increments while maximizing the accuracy. One of the quickest ways to limit the computational intensity is to keep the solution scale as high as possible, i.e., large increments. The incremental approach has the greatest effect when geometric nonlinearities are more significant. In the first deformation case, there was a significant effect with the FID alignment, where the model must resolve the rigid registration between Fig. 8(a) and (c) in addition to the large shift, which is on the order of 3 cm in some areas. There are limited effects from the solution scale for ICP-WHOLE, ICP-PARTIAL, and DIRR-WHOLE, since there is less shift to resolve. In each of these three alignments, the lowest mean tumor error occurred at a solution scale less than 1. While the mean tumor error for these alignments varied less than 0.5 mm over the full range of solution scale values, there were some instances of individual tumor errors improving 1–2 mm. Finally, there were adverse effects for the DIRR-PARTIAL alignment. In this case, as mentioned above, there was a slight misalignment, which compounded with the incremental approach. The solution scale had very little effect on the smaller deformations observed in the second deformation case, as there are less issues with determining correspondence.

Another way to reduce computation time is to eliminate the steps where the stiffness matrix was rebuilt. From the results of Fig. 11, there was a decrease in targeting accuracy when implementing this time-saving tactic, mainly at the tumors where the most shift was present. The error was also higher when using a static grid and rebuilding the stiffness matrix with updated surface normals to preserve mesh quality. However, when aligning the surface with ICP, these measures became more effective.

Since the model is primarily driven by intraoperative data, the method by which boundary conditions are chosen for each node can play a significant role in the resulting accuracy. If nodes that are specified to have closest point boundary conditions are located where there is minimal coverage provided by intraoperative data, inaccurate values for boundary conditions could result. One way to limit these inaccuracies is to use RBF fitting to construct a distance map associated with the intraoperative data, providing a more complete representation of the data and accurate closest point distance calculations for the boundary conditions at the cost of greater preprocessing time. In this study, we attempted to determine if the deformation could be identified and corrected from partial surface data alone. However, we have the capability to acquire subsurface information intraoperatively using coregistered ultrasound [54], which could improve the accuracy of this method.

Considering the numerous amount of nonrigid registration algorithms available, it might seem more intuitive to implement one of these methods instead. In fact, deformable algorithms that use feature and geometric information are being considered in future studies as a means of comparison. The main challenge that arises with many of these methods is how to deform the preoperative mesh in regions where there is no intraoperative data present to provide corresponding features to drive the nonrigid algorithm. Using fixed boundary conditions to hold these regions immobile does not accurately represent the deformation that is occurring in the operating room. In fact, most of the boundary on the underside of the phantom or the liver is allowed to deform and is prescribed stress-free boundary conditions. This method appears to be more intuitive than to modify a nonrigid transformation to simulate stress-free boundary conditions in areas where the intraoperative data is incomplete.

Arguably though, the advantage of FEM-based compensation is that the deformation behavior can be grounded within an analysis of the continuum as relayed within a partial differential equation describing elastic mechanics. As a result, compensation is based on the physics of deformation rather than a process of polynomial interpolation. While it is true that polynomial basis functions are often at the core of FEM, the process of prescribing the correct boundary conditions for modeling deformation has a distinct link to physical quantities such as displacement, strain, force, and stress.

### C. The Role of Surface Coverage

The incomplete surface data seems to provide the largest challenge for developing the model-updated framework. If the partial coverage of the range scanner is uneven and does not capture enough points over the minimally deformed region, then the cost function of (2) will result in values different from those acquired with a complete, uniformly sampled description, as obtained from the CT data. This uneven coverage could lead to a shift in the location of the desired minimum. As a result, this alignment could have inaccuracies with regards to identifying deformation and establishing accurate correspondence. The same effect is also observed when using only the minimally deformed regions of the partial range scan surface in an ICP registration.

In the first deformation case, the DIRR-PARTIAL algorithm results in a slight rotation normal to the deformation in the first case. This rotation places the ridge of the intraoperative data over the wrong area of the surface. As a result, the correspondences are incorrect and improper values are used for the boundary conditions, leading to higher inaccuracies than other initial alignments. The second deformation case shows another challenge regarding intraoperative data acquisition that involves accurately capturing the deformation. Both range scans were acquired from the top view of the phantom, while much of the deformation in the second case is occurring at the inferior ridge. If range scan data would have been more focused on the site of deformation, the algorithms would have performed better.

While partial surface data can have a significant effect on identifying and subsequently correcting for deformation, the uneven coverage is a more important issue. Simulated range scans were created by taking the CT data from deformed sets and eliminating the points representing the bottom region of the phantom. Initial studies using these data sets show good convergence with the DIRR. For the first deformation case, a successful registration, as defined in Section II, was 99.6% over 1000 trials using the simulated range scans, and 96.5% for the second case. Both data sets were closer to the results provided by the complete CT sets than the range scan surfaces. This data can be used in the future to determine the effects of coverage on the DIRR and deformable models.

## V. Conclusion

We have developed a method for identifying and compensating shift using only surface data. The goal of the DIRR was to provide the same rigid registration that would occur if only the minimally deformed regions of the surface were used. The DIRR accomplished this objective to within 2 mm when using a complete description of a deformed surface and 4 mm for a partial surface. The finite element model resulted in improvements over the rigid registration when closest point boundary conditions were represented in a normal-tangential framework. The incremental approach had a modest effect for cases of large deformations. The model achieved the best accuracies when initial alignments were provided from complete descriptions of the deformed surface (ICP-WHOLE, DIRR-WHOLE). However, the FEM also performed better when aligned using DIRR compared to ICP alignment for both representations of the deformed surface (complete CT and partial range scan).

## Acknowledgment

Most of the registration and visualization algorithms were developed using the Visualization Toolkit (www.vtk.org). The authors would like to acknowledge FarField Technology for the aid in the use of their surface fitting software based on RBFs. Some segmentation and calculation were performed using Analyze AVW Version 3.1–Biomedical Resource, provided in collaboration with the Mayo Foundation, Rochester, MN. Phantom images were acquired with the CT technicians at Vanderbilt Medical Center's Department of Radiology.

## References

[1] B. Horn, "Closed-form solution of absolute orientation using unit quaternions," *J. Opt. Soc. Amer.*, vol. 4, pp. 629–642, 1987.

[2] P. H. Schonemann, "A generalized solution of the orthogonal procrustes problem," *Psychometrika*, vol. 31, pp. 1–10, 1966.

[3] K. Arun, T. Huang, and S. D. Blostein, "Least-squares fitting of 2 3-D point sets," *IEEE Trans. Pattern Anal. Mach. Intell.*, vol. 9, no. 5, pp. 699–700, Sep. 1987.

[4] D. Roberts, A. Hartov, F. Kennedy, M. Miga, and K. Paulsen, "Intraoperative brain shift and deformation: A quantitative analysis of cortical displacement in 28 cases," *Neurosurgery*, vol. 43, no. 4, pp. 749–758, Oct. 1998.

[5] D. Hill, C. Maurer, R. Maciunas, J. Barwise, J. Fitzpatrick, and M. Wang, "Measurement of intraoperative brain surface deformation under a craniotomy," *Neurosurgery*, vol. 43, no. 3, pp. 514–526, 1998.

[6] A. Nabavi, P. Black, D. Gering, C. Westin, V. Mehta, R. Pergolizzi, M. Ferrant, S. Warfield, N. Hata, R. Schwartz, W. Wells, R. Kikinis, and F. Jolesz, "Serial intraoperative magnetic resonance imaging of brain shift," *Neurosurgery*, vol. 48, no. 4, pp. 787–797, 2001.

[7] C. Nimsky, O. Ganslandt, S. Cerny, P. Hastreiter, G. Greiner, and R. Fahlbusch, "Quantification of, visualization of, and compensation for brain shift using intraoperative magnetic resonance imaging," *Neurosurgery*, vol. 47, no. 5, pp. 1070–1079, 2000.

[8] C. R. Maurer, D. L. G. Hill, A. J. Martin, H. Y. Liu, M. McCue, D. Rueckert, D. Lloret, W. A. Hall, R. E. Maxwell, D. J. Hawkes, and C. L. Truwit, "Investigation of intraoperative brain deformation using a 1.5-T interventional mr system: Preliminary results," *IEEE Trans. Med. Imag.*, vol. 17, no. 5, pp. 817–825, Oct. 1998.

[9] R. Szeliski and S. Lavallee, "Matching 3-D anatomical surfaces with nonrigid deformations using octree-splines," *Int. J. Comput. Vis.*, vol. 18, no. 2, pp. 171–186, 1996.

[10] M. Audette, K. Siddiqi, F. Ferrie, and T. Peters, "An integrated range-sensing, segmentation and registration framework for the characterization of intra-surgical brain deformations in image-guided surgery," *Comput. Vis. Image Understanding*, vol. 89, no. 2–3, pp. 226–251, 2003.

[11] H. Chui and A. Rangarajan, "A new point matching algorithm for nonrigid registration," *Comput. Vis. Image Understanding*, vol. 89, pp. 114–141, 2003.

[12] J. Feldmar and N. Ayache, "Rigid, affine and locally affine registration of free-form surfaces," *Int. J. Comput. Vis.*, vol. 18, no. 2, pp. 99–119, 1996.

[13] P. Laskov and C. Kambhamettu, "Curvature-based algorithms for nonrigid motion and correspondence estimation," *IEEE Trans. Pattern Anal. Mach. Intell.*, vol. 25, no. 10, pp. 1349–1354, Oct. 2003.

[14] C. Kambhamettu, D. Goldgof, M. He, and P. Laskov, "3-D nonrigid motion analysis under small deformations," *Image Vis. Computing*, vol. 21, no. 3, pp. 229–245, 2003.

[15] D. Meier and E. Fisher, "Parameter space warping: Shape-based correspondence between morphologically different objects," *IEEE Trans. Med. Imag.*, vol. 21, no. 1, pp. 31–47, Jan. 2002.

[16] P. Shi, A. Sinusas, T. Constable, E. Ritman, and S. Duncan, "Point-tracked quantitative analysis of left ventricular surface motion from 3-D image sequences," *IEEE Trans. Med. Imag.*, vol. 19, no. 1, pp. 36–50, Jan. 2000.

[17] S. Aylward, J. Jomier, J.-P. Guyon, and S. Weeks, "Intra-operative 3D ultrasound augmentation," in *Proc. 2002 IEEE Int. Symp. Biomedical Imaging*, 2002, pp. 421–424.

[18] A. P. King, J. M. Blackall, G. P. Penney, and D. J. Hawkes, "Tracking liver motion using 3-D ultrasound and a surface-based statistical shape model," in *Proc. IEEE Workshop Mathematical Methods in Biomedical Image Analysis*, 2001, pp. 145–152.

[19] J. M. Blackall, G. P. Penney, A. P. King, A. N. Adam, and D. J. Hawkes, "Tracking alignment of sparse ultrasound with preoperative images of the liver and an interventional plan using models of respiratory motion and deformation," in *Proc. SPIE Medical Imaging 2004: Visualization, Image-Guided Procedures, and Display*, vol. 5367, 2004, pp. 218–227.

[20] M. Miga, K. Paulsen, J. Lemery, S. Eisner, A. Hartov, F. Kennedy, and D. Roberts, "Model-updated image guidance: Initial clinical experiences with gravity- induced brain deformation," *IEEE Trans. Med. Imag.*, vol. 18, no. 10, pp. 866–874, Oct. 1999.

[21] M. Miga, K. Paulsen, F. Kennedy, P. Hoopes, A. Hartov, and D. Roberts, "A 3D brain deformation model experiencing comparable surgical loads," in *Proc. 19th Annu. Int. Conf. IEEE Engineering in Medicine and Biology Society*, vol. 2, 1997, pp. 773–776.

[22] M. Miga, D. Roberts, F. Kennedy, L. Platenik, A. Hartov, K. Lunn, and K. Paulsen, "Modeling of retraction and resection for intraoperative updating of images," *Neurosurgery*, vol. 49, no. 1, pp. 75–84, Jul. 2001.

[23] M. Ferrant, A. Nabavi, B. Macq, F. Jolesz, R. Kikinis, and S. Warfield, "Registration of 3-D intraoperative mr images of the brain using a finite-element biomechanical model," *IEEE Trans. Med. Imag.*, vol. 20, no. 12, pp. 1384–1397, Dec. 2001.

[24] O. Skrinjar, A. Nabavi, and J. Duncan, "Model-driven brain shift compensation," *Med. Image Anal.*, vol. 6, no. 4, pp. 361–373, Dec. 2002.

[25] K. E. Lunn, K. D. Paulsen, D. W. Roberts, F. E. Kennedy, A. Hartov, and L. A. Platenik, "Nonrigid brain registration: Synthesizing full volume deformation fields from model basis solutions constrained by partial volume intraoperative data," *Comput. Vis. Image Understanding*, vol. 89, pp. 299–317, 2003.

[26] K. S. Hughes, R. Simon, and S. Songhorabodi *et al.*, "Resection of the liver for colorectal-carcinoma metastases – A multiinstitutional study of patterns of recurrence," *Surgery*, vol. 100, pp. 278–284, 1986.

[27] A. J. Herline, J. L. Herring, J. D. Stefansic, W. C. Chapman, R. L. Galloway, and B. M. Dawant, "Surface registration for use in interactive image-guided liver surgery," in *Lecture Notes in Computer Science*. Berlin, Germany: Springer-Verlag, 1999, vol. 1679, : Medical Imaging Computation and Computer-Assisted Intervention: MICCAI '99, pp. 892–899.

[28] P. J. Besl and N. D. McKay, "A method for registration of 3-D shapes," *IEEE Trans. Pattern Anal. Mach. Intell.*, vol. 14, no. 2, pp. 239–256, Feb. 1992.

[29] D. M. Cash, T. K. Sinha, W. C. Chapman, H. Terawaki, B. M. Dawant, R. L. Galloway, and M. I. Miga, "Incorporation of a laser range scanner into image-guided liver surgery: Surface acquisition, registration, and tracking," *Med. Phys.*, vol. 30, no. 7, pp. 1671–1682, Jun. 2003.

[30] M. Miga, D. Cash, Z. Cao, R. L. Galloway, B. Dawant, and W. Chapman, "Intraoperative registration of the liver for image-guided surgery using laser range scanning and deformable models," *Proc. SPIE Medical Imaging 2003*, vol. 5029, 2003.

[31] D. M. Cash, T. Sinha, C. C. Chen, B. M. Dawant, W. C. Chapman, M. I. Miga, and R. L. Galloway, "Identification of deformation using invariant surface information," *Proc. SPIE Medical Imaging 2004*, vol. 5367, pp. 140–150, 2004.

[32] G. P. Penney, J. M. Blackall, M. S. Hamady, T. Sabharwal, A. Adam, and D. Hawkes, "Registration of freehand 3D ultrasound and magnetic resonance liver images," *Med. Image Anal.*, vol. 8, pp. 81–91, 2004.

[33] K. M. Brock, J. M. Balter, L. A. Dawson, M. L. Kessler, and C. R. Meyer, "Automated generation of a four-dimensional model of the liver using warping and mutual information," *Med. Phys.*, vol. 30, no. 6, pp. 1128–1133, Jun. 2003.

[34] T. Rohlfing, C. R. Maurer, W. G. O'Dell, and J. H. Zhong, "Modeling liver motion and deformation during the respiratory cycle using intensity-based nonrigid registration of gated MR images," *Med. Phys.*, vol. 31, no. 3, pp. 427–432, Mar. 2004.

[35] S. Shimizu, B. Shirato, B. Xo, K. Kagei, T. Nishioka, S. Hashimoto, K. Tsuchiya, H. Aoyama, and K. Miyasaka, "Three-dimensional movement of a liver tumor detected by high- speed magnetic resonance imaging," *Radiother. Oncol.*, vol. 50, no. 3, pp. 367–370, 1999.

[36] H. Korin, R. Ehman, S. Riederer, J. Felmlee, and R. Grimm, "Respiratory kinematics of the upper abdominal organs: A quantitative study," *Magn. Reson. Med.*, vol. 23, no. 1, pp. 172–178, Jan. 1992.

[37] I. Suramo, M. Paivansalo, and V. Myllyla, "Cranio-caudal movements of the liver, pancreas and kidneys in respiration," *Acta Radiol. Diagn. (Stockholm)*, vol. 25, no. 2, pp. 129–131, 1984.

[38] C. Couinaud, *Le Foie: Etudes Anatomiques et Chirurgicales*. Paris, France: Masson, 1957, Original definition of Couinaud segments for liver.

[39] W. H. Press, S. A. Teukolsky, W. T. Vetterling, and B. P. Flannery, *Numerical Recipes in C: The Art of Scientific Computing*, 2nd ed. New York: Cambridge Unive. Press, 1992.

[40] The VXL Homepage – C++ Libraries for Computer Vision Research and Implementation. VXL. [Online]. Available: http://vxl.sourceforge.net/

[41] J. Carr, B. Beatson, R. K. adn McCallum, W. Fright, T. McLennan, and T. Mitchell, "Smooth surface reconstruction from noisy range data," in *Proc. ACM GRAPHITE 2003*, Melbourne, Austraila, 2003, pp. 119–126.

[42] S. Pan and B. M. Dawant, "Automatic 3D segmentation of the liver from abdominal CT images: A level-set approach," *Proc. SPIE Medical Imaging 2001: Image Processing*, vol. 4322, pp. 128–138, 2001.

[43] Z. Cao, S. Pan, L. Hermoye, and B. Dawant, "The accumulative speed function: A new level set based segmentation technique with an application to mr liver segmentation," *IEEE Trans. Med. Imag.*, to be published.

[44] W. Lorensen and H. Cline, "Marching cubes: A high resolution 3D surface construction algorithm," *ACM Comput. Graphics*, vol. 21, no. 4, pp. 163–169, Jul. 1987.

[45] J. Sullivan, G. Charron, and K. Paulsen, "A three-dimensional mesh generator for arbitrary multiple material domains," *Finite Elements Anal. Design*, vol. 25, no. 3–4, pp. 219–241, 1997.

[46] M. S. Engelman and R. Sani, "The implementation of normal and/or tangential boundary conditions in finite element codes for incompressible fluid flow," *Int. J. Numerical Meth. Fluids*, vol. 2, pp. 225–238, 1982.

[47] L. A. Platenik, M. I. Miga, D. Roberts, K. E. Lunn, F. E. Kennedy, A. Hartov, and K. D. Paulsen, "In vivo quantification of retraction deformation modeling for updated image-guidance during neurosurgery," *IEEE Trans. Biomed. Eng.*, vol. 49, no. 8, pp. 823–835, Aug. 2002.

[48] S. Balay, W. D. Gropp, L. C. McInnes, and B. F. Smith, *Efficienct Management of Parallelism in Object Oriented Numerical Software Libraries*. Cambridge, MA: Birkhauser, 1997, pp. 163–202.

[49] Y. Saad and M. H. Schultz, "GMRES: A generalized minimal residual algorithm for solving nonsymmetric linear systems," in *SIAM J. Sci. Statist. Comput.*, vol. 7, 1986, pp. 856–869.

[50] J. Fitzpatrick, J. West, and C. Maurer, "Predicting error in rigid-body point-based registration," *IEEE Trans. Med. Imag.*, vol. 17, no. 5, pp. 694–702, Oct. 1998.

[51] A. E. Johnson and S. B. Kang, "Registration and integration of textured 3D data," *Image Vis. Comput.*, vol. 17, no. 2, pp. 135–147, Feb. 1999.

[52] G. Sharp, S. Lee, and D. Wehe, "ICP registration using invariant features," *IEEE Trans. Pattern Anal. Mach. Intell.*, vol. 24, no. 1, pp. 90–102, Jan. 2002.

[53] G. Godin, D. Laurendeau, and R. Bergevin, "A method for the registration of attributed range images," in *Proc. 3DIM 2001*, May 2001, pp. 179–186.

[54] P. Bao, J. Warmath, R. L. Galloway, and A. Herline, "Ultrasound to CT registration for image-guided laparoscopic liver surgery," Surgical Endosc., 2004, to be published.